MECHANICAL AND MICROSTRUCTURAL ASPECTS OF DECREPITATION IN INTERMETALLIC HYDROGEN STORAGE MATERIALS

Emeline CHEVALLIER[a], Yves GAILLARD[a], Ioana POPA[b], David CHAPELLE[a], Anne MAYNADIER[a]

a Université Marie et Louis Pasteur, CNRS, institut FEMTO-ST, F-25000 Besançon, France
b ICB, UMR 6303 CNRS-Université Bourgogne Europe, 21078 DIJON, France
*Corresponding author: E-mail: anne.maynadier@femto-st.fr.

ABSTRACT

This study addresses the challenges associated with hydrogen storage as part of the transition toward low-carbon energy systems. Among available solutions, solid-state hydrogen storage in intermetallic compounds offers promising advantages, although it is limited by mechanical aging phenomena such as decrepitation. Three intermetallic materials ($LaNi_5$, $TiFe_{0.9}Mn_{0.1}$, and $TiMn_{1.5}$) are investigated to better understand the relationship between microstructure, mechanical properties, and particle fragmentation. Microstructural and compositional analyses revealed significant deviations from ideal single-phase structures, with multiphase compositions attributed to industrial processing conditions. Nanoindentation results highlighted heterogeneous mechanical behavior, particularly in $TiMn_{1.5}$, suggesting a link between local mechanical properties and crack-aging initiation.

INTRODUCTION

As greenhouse gas emissions rise, energy demand grows, and fossil resources are depleted, the transition towards cleaner energy alternatives has become a major challenge. The three main renewable energy sources - hydroelectricity, solar, and wind - offer promising solutions for reducing CO_2 emissions. However, only hydroelectricity is dispatchable; the others remain intermittent, highlighting the need for efficient energy storage solutions. In this context, hydrogen has emerged as a promising energy carrier. Although currently used mainly in oil refining and ammonia production, its potential is expanding toward applications such as industrial decarbonization and large-scale energy storage [1].

When not produced near its point of use, hydrogen must be stored and transported. Its low volumetric energy density requires compression or liquefaction, involving extreme conditions (700 bar or -273 °C) with associated challenges in cost, safety, and energy efficiency [1]. Solid-state storage in intermetallic compounds offers an alternative: hydrogen is absorbed into the crystal lattice, forming a solid solution (α phase) that transitions to a hydride compound (β phase), with reversible absorption and desorption near ambient conditions [2].

This hydriding process involves a significant volume change in the crystal unit cell - up to 36% in some compounds [3] - which induces mechanical stresses that cause particle fragmentation, known as decrepitation. Fine particles progressively fill the void spaces within the powder bed, reducing porosity and limiting further expansion during subsequent cycles. As a result, particles push against the vessel walls, generating stresses that can lead to visible and damaging permanent strain [4,5]. Despite being widely observed, the underlying mechanisms of decrepitation remains insufficiently understood. This study examines the mechanical, microstructural, and compositional characteristics of three intermetallic compounds to elucidate the microstructural mechanisms driving decrepitation.

MATERIALS

Intermetallic, with the general formula AB_n, combine an element A that easily forms very stable metal hydrides with an element B that forms very unstable hydrides, requiring very high pressure. Enabling the formation of hydrides with intermediate stability and promoting reversibility [2] is a challenge. In this study, the selected materials are three yet industrially implemented intermetallic alloys: $LaNi_5$, $TiMn_{1.5}$, and $TiFe_{0.9}Mn_{0.1}$. The alloys are supplied by the company FHYBERA (Dole,

France) and synthesized by vacuum induction melting. According to the supplier, material purity ranges between 99.9 and 99.95%. The samples are used in the as-cast state, without any homogenization or annealing treatment. Jaw crushing is also carried out by the company, under air atmosphere.

$LaNi_5$

$LaNi_5$ belongs to the AB_5 family and crystallizes in a hexagonal $CaCu_5$-type structure (P6/mmm, a ≈ 5.017 Å, c ≈ 3.987 Å) [6]. It offers high volumetric density (115 kg $H_2.m^{-3}$), relatively easy activation, fast kinetics, and a moderate plateau pressure [7,8].

First hydrogenation, the activation, requires elevated pressure (≥ 10 bar) and temperature, after which the alloy exhibits fast and reversible kinetics [7]. However, $LaNi_5$ undergoes pronounced ageing. After 100 cycles at 40°C, maximum storage capacity drops from 1.5 wt% to 1 wt%, trapped hydrogen increases, and Pressure-Composition-Isotherm (PCI) curves show rising desorption plateau pressure and increasing hysteresis [8]. This ageing is generally accompanied by decrepitation into very fine powder [4].

$TiFe_{0.9}Mn_{0.1}$

$TiFe_{0.9}Mn_{0.1}$ is derived from TiFe, an AB-type intermetallic with low cost, good reversibility, and recyclability. Literature reports experimentally identified maximal storage capacity rather around 1.7 wt% (1.72 wt% at 30°C and 62 bar [9]; 1.69wt% at 25°C and 58 bar [10]). TiFe crystallizes in a CsCl-type cubic structure (Pm-3m, a ≈ 2.9437 Å) (see phase diagram in [2]) and forms two successive hydrides (β-$TiFeH_{1.04}$ and γ-$TiFeH_{1.9}$) with a total lattice volume expansion of 18% [11].

Its main limitations are difficult activation (requiring up to 400°C and 65 bar) and a second transformation plateau when wt%H > 1.04, restricting its practical use. Partial substitution of Fe by Mn and non-stoichiometric compositions facilitate activation conditions and lower equilibrium pressures [12,13], which motivated the selection of $TiFe_{0.9}Mn_{0.1}$ here. Dematteis *et al.* reports a maximal capacity of 1.75 wt% at 25 °C and 79 bar [2] .
This compound is TiFe-like, essentially single-phase (CsCl), though some secondary phases as $TiFe_2$ or βTi can appear, surface oxides may also be present [2,14]. Increasing manganese content decreases absorption plateau pressures without significantly affecting maximum capacity, but increases plateau slope, which can be mitigated by homogenization annealing [13].

$TiMn_{1.5}$

$TiMn_{1.5}$ belongs to the AB_2 family, known for high gravimetric capacity, good cycling stability, fast room-temperature kinetics, and low cost. It crystallizes predominantly in the hexagonal C14 Laves phase ($P6_3/mmc$) at high temperature [15], but present many secondary phases. A detailed phase diagram can be found in [16].

$TiMn_{1.5}$ does not require activation treatment, though surface oxide removal may occasionally be needed [17]. PCI curves show a maximum capacity of 1 H/M, around 1.8 wt% at room temperature, with a sloped absorption plateau reducible by homogenization annealing [18]. Ageing occurs through lattice expansion, heterogeneous stress build-up, and irreversible hydrogen trapping in δ-TiH hydrides, leading to increased PCI slope and reduced storage capacity over cycling [19,20].

METHODS

Scanning electron microscopy (SEM) was used to investigate the microstructure of the as-cast materials in form of powder.

Energy-dispersive spectroscopy (EDS), typically coupled with SEM, was used to determine the elemental composition of materials through the detection of characteristic X-rays. It enables semi-quantitative elemental identification, and it was useful for mapping element distribution, detecting compositional heterogeneities, and verifying alloy stoichiometry. Atomic percentages were normalized to 100 %.

Nanoindentation is used to measure the local mechanical properties of materials, such as hardness H and apparent elastic modulus E_{app}, at the nanometric scale. In this study an Ultra-Nano Indentor CSM was used with a Berkovich tip. Analysis of the load–displacement curves allow mechanical properties to be extracted, while performing indentation grid enables the mapping of H and E_{app} at the microstructural scale.

RESULTS AND DISCUSSION

Microstructural and elemental analysis

Microstructural and elemental analysis of the intermetallic compounds are essential to understand

the mechanisms responsible for decrepitation and hydrogen storage properties, as hydriding depends on the organization of the principal, secondary phases and grain boundaries, some of which may promote crack formation upon hydrogen exposure.

$LaNi_5$

Figure 1 shows a SEM micrograph (BSE) of $LaNi_5$. Contrary to phase diagram predictions, the sample exhibits two main phases: a light grey matrix and an eutectic structure of light and dark grey regions, consistent with Ni-rich La–Ni eutectics. A few sparse white dots are also observed. Some, long intragranular cracks, bypassing the eutectic phase, are present, most likely generated during particle milling.

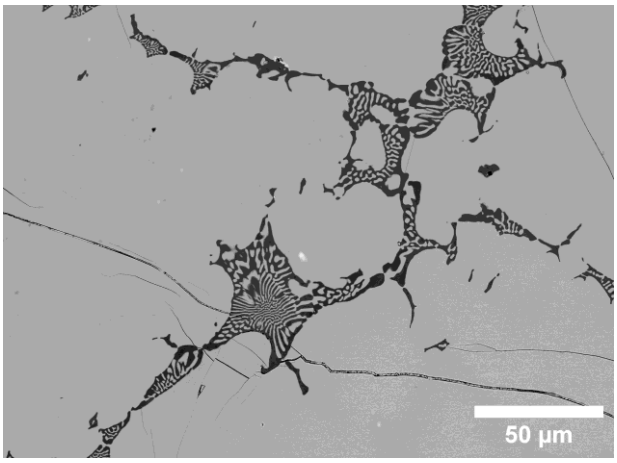

Figure 1. SEM micrograph of $LaNi_5$: large domains of uniform preponderant phase while secondary eutectic phase seems present at grain boundaries.

Five EDS composition analysis ($t_{count} \approx 50$ s at 15 kV) are reported in Table 1corresponding to 5 zones: the matrix (zone 1), the eutectic (zone 2), its light grey lamellae within the eutectic (zone 3), dark grey lamellae within the eutectic (zone 4), and white dots (zone 5).

The use of mischmetal (45–50% Ce, 25% La, 15–20% Nd, 5% Pr) rather than pure lanthanum (La) for this synthesis, explains the presence of Ce, Nd, and Pr in the elemental analyses; these were treated as lanthanum for comparison with phase diagram predictions.

Table 1: EDS composition analysis (50 s at 15 kV) on $LaNi_5$ sample: composition is reported in at%.

Zone	O	Al	S	Fe	Ni	RE*
1		2.0			80.7	17.3
2	0.8	13.2	0.1		78.4	7.5
3	0.4	4.0			80.2	15.4
4	0.7	19.4	0.2	0.4	77.8	1.5
5	46.6	1.1	1.6		20.9	29.8

**RE: Rare earths such as La, Ce, Pr and Nd*

The matrix composition is broadly consistent with $LaNi_5$, with 2 at% Al detected. The eutectic regions show significantly higher Al concentration (13 at%), indicating preferential probable segregation of Al in grain boundaries. Higher-magnification analysis reveals that Al is concentrated in the dark grey lamellae of the eutectic phase (19 at%), which is likely to displays a microstructure reminiscent of nickel-based superalloys. Minor impurities (S, O, Fe) were also detected, with uncertain origins, possibly linked to raw nickel impurities or the use of recycled materials. The light grey lamellae have a composition close to $LaNi_5$ with a lower Al content (4 at%) in substitution of Ni. The white spots likely correspond to La–Ni oxides.

$TiFe_{0.9}Mn_{0.1}$

Figure 2 shows a SEM micrograph (BSE) of $TiFe_{0.9}Mn_{0.1}$. Unlike the single-phase material typically reported in the literature, the sample is multiphase, with four main phases: a grey matrix (zone 1), a white phase (zone 2), a dark grey phase (zone 3), a very dark grey phase (zone 4), and a black phase (zone 5).

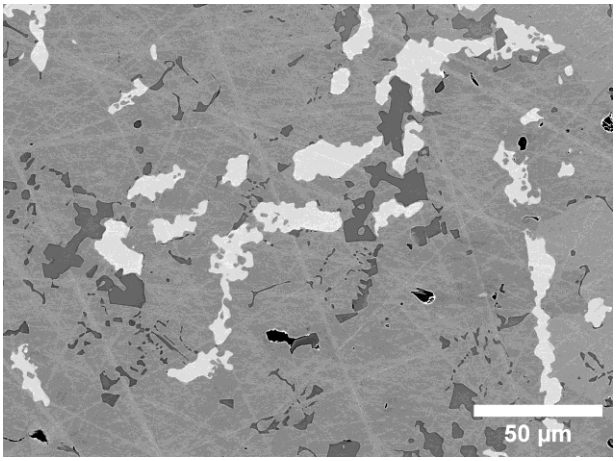

Figure 2. SEM micrograph of $TiFe_{0.9}Mn_{0.1}$ revealing four distinct phases, where grey-level contrast reflects compositional heterogeneity.

Table 2: EDS composition analysis (50 s at 15 kV) on $TiFe_{0.9}Mn_{0.1}$ sample: composition is reported in at%.

Zone	O	Al	Si	S	Ti	Mn	Fe	Zr
1		0.2			50.5	4.9	44.3	0.1
2		0.2			40.6	7.0	52.1	0.1
3	12.0				51.4	3.8	32.6	0.2
4	4.1	0.4	1.0	4.8	63.2	7.1	17.7	1.7
5		0.7		3.3	82.8	3.8	4.6	4.8

The matrix is close in composition to $TiFe_{0.9}Mn_{0.1}$. The white phase is iron-enriched and titanium-depleted, with a dendritic morphology. The dark grey phases are titanium-enriched and iron-depleted, with notable oxygen content (up to 12 at%) and minor impurities (S, Si), not homogeneously distributed. Trace of Al and Zr were also detected locally, with the Zr possibly related to melting contamination. The black phase likely corresponds to titanium-rich precipitates.

$TiMn_{1.5}$

Figure 3 shows a SEM micrograph (BSE) of $TiMn_{1.5}$. Contrary to the expected two-phase structure ($TiMn_2$ + minority TiMn) typically reported in the literature, the sample exhibits four phases: the matrix (zone 1), a light grey phase (zone 2), a dark grey phase (zone 3), and a black phase (zone 4).

The matrix is close to the expected $TiMn_{1.5}$ composition. The light grey phase is titanium-enriched and manganese-depleted, the dark grey phase shows comparable Ti and Mn contents with a slight Ti predominance and higher oxygen concentration, and the black zones are titanium-rich and manganese-depleted, with impurities including S and Se with uncertain origins.

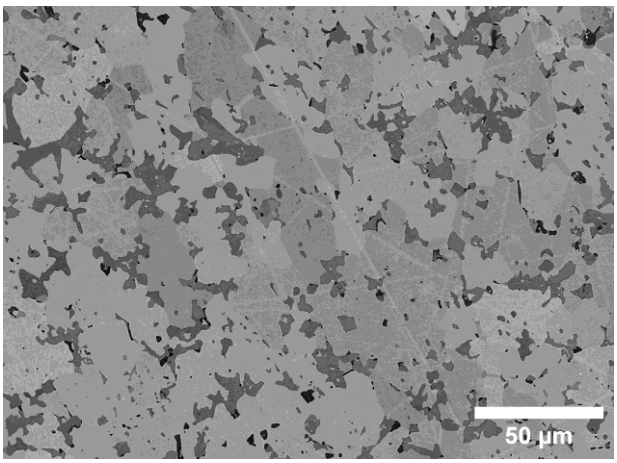

Figure 3. SEM micrograph of $TiFeMn_{1.5}$ revealing four distinct phases, where grey-level contrast reflects compositional heterogeneity.

Table 3: EDS composition analysis (50 s at 15 kV) on $TiMn_{1.5}$ sample: composition is reported in at%.

Zone	O at%	Al at%	S at%	Ti at%	Mn at%	Se at%
1		0.2		38.2	61.6	
2	11.6	0.1		46.7	41.6	
3	7.8	0.1		48.0	44.1	
4	14.2	0.1	1.6	56.1	27.3	0.7

In conclusion, all three samples deviate from phase diagram predictions and literature results, exhibiting multiphase microstructures with varying compositions. This is attributed to the processing conditions: unlike small-scale academic studies involving remelting and homogenization treatments, these materials were industrially produced in large quantities without post-processing heat treatment, favoring the formation of chemical and structural heterogeneities.

Nano-indentation

Nanoindentation is employed to characterize the local mechanical properties. The aim is to map E_{app} and H, in order to identify a potential correlation between these properties and microstructure associated with decrepitation. This approach also aims to evaluate the ability of certain phases to accommodate — or not — the stresses induced by volume changes during hydrogen absorption.

This section presents preliminary nanoindentation grids obtained on particles of $TiFe_{0.9}Mn_{0.1}$ and $TiMn_{1.5}$ (with sizes ranging from 1 to 2 mm), embedded in a carbon-filled conductive resin. The results are reported as colored pixelwise maps, where white pixels correspond to erroneous outlier measurements.

For $TiFe_{0.9}Mn_{0.1}$, the results (H in Figure 4 and E_{app} in Figure 5) correspond to 300-indent grid (15 × 20) over 760 x 560 µm area, spanning 38 µm. No significant contrast in mechanical properties is observed, either in Ea_{pp} or H, with the exception of a few isolated data points.

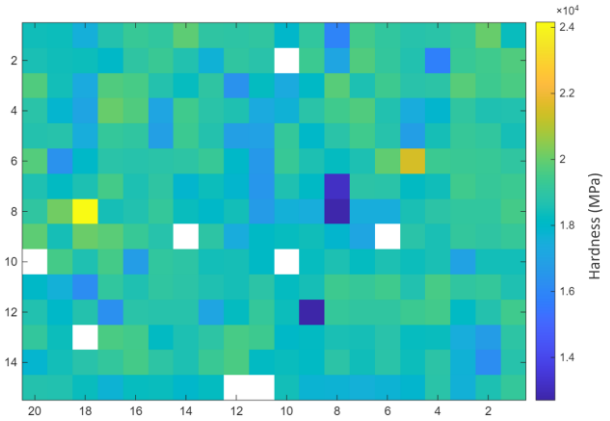

Figure 4. Hardness H.

Several factors may account for this observation. On one hand, the small size of the phases (below 20 µm), their irregular morphology, and the short spacing between indents make it difficult to consistently position indents within individual phases, limiting the representativeness of the measurements. Moreover, as some phases are expected to have similar structure but slightly different chemical compositions due to Mn migration, their mechanical properties may also be quite similar, potentially masking any existing differences.

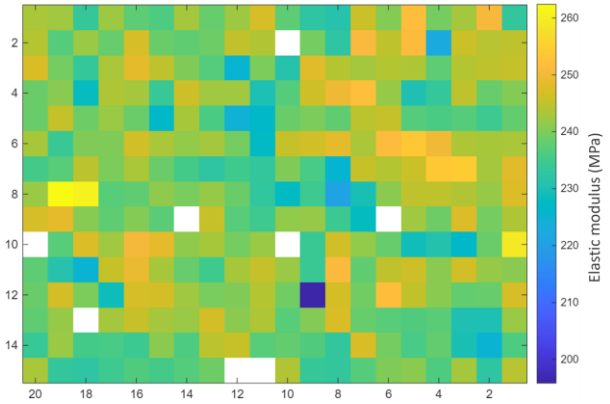

Figure 5. Apparent elastic modulus E_{app}.

The maps obtained for $TiMn_{1.5}$ (hardness in Figure 6 and apparent elastic modulus in Figure 7) correspond to 400-indent grid (20 × 20) over 38 x 38 µm area, spanning ~ 2 µm. They appear more contrasted.

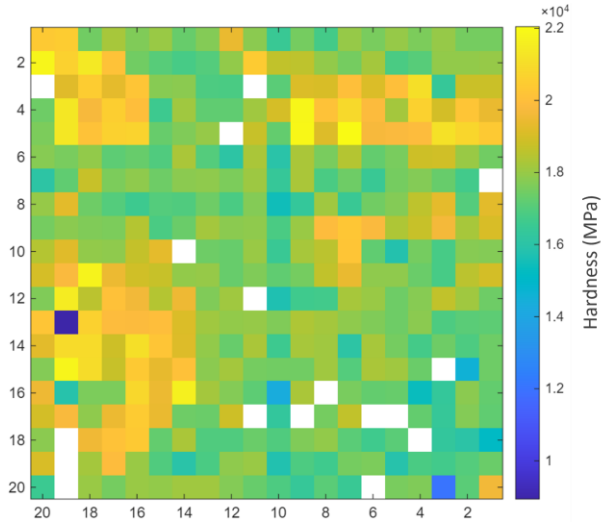

Figure 6. Hardness H.

In particular, the elastic modulus map reveals two distinct populations: one associated with values between 160 and 220 MPa (shown in blue), and another corresponding to values higher than 230 MPa (shown in yellow). This distribution appears to correlate with the phases observed in the EDS composition analysis, suggesting mechanical differentiation between these phases. In contrast, the hardness distribution appears more homogeneous and does not clearly distinguish between the different zones, indicating that this parameter is less sensitive to microstructural variations in this material.

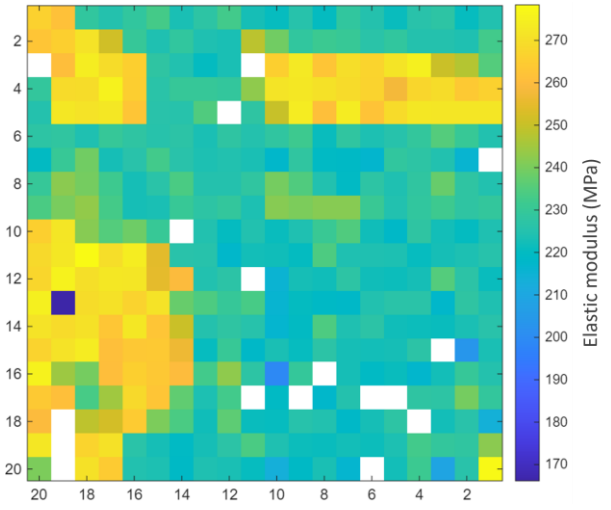

Figure 7. Apparent elastic modulus E_{app}.

CONCLUSIONS

The present study selected three intermetallic compounds: $LaNi_5$, $TiFe_{0.9}Mn_{0.1}$ and $TiMn_{1.5}$. A combination of SEM, EDS and nanoindentation was

employed to analyze their microstructural, compositional and mechanical properties.

The results demonstrated that materials exhibit multiple phases with distinct chemical composition. Nanoindentation results reveal a significant correlation between composition and mechanical properties, particularly for $TiMn_{1.5}$, whereas the results for $TiFe_{0.9}Mn_{0.1}$ are less contrasted and do not allow for establishing a clear relationship.

Future work will focus on nanoindentation mapping following EBSD analyses to assess the influence of crystallographic orientation on mechanical properties, as well as exposing intermetallic compounds to hydrogen to investigate storage properties and decrepitation behavior through granulometry.

KEYWORDS

Intermetallic compounds; solid-state storage; hydrogen storage; nanoindentation; decrepitation; microstructural characterization.

ACKNOWLEDGMENTS

This work has been supported by the EIPHI Graduate School (contract ANR-17-EURE-0002), the Region Bourgogne Franche-Comté (CYCLAHMID Project) and by the French RENATECH network and its FEMTO-ST technological facility. The authors would like to thank the AMETISTE platform for access to the equipment.

REFERENCES

[1] Beauger, C., Nobrega, P. H. A., Jodry, A., Hassen, F. H., Ahmar, E. E., Pérez-López, P., Schlesinger-Martinat, J., Akrich, M., Mallard, A., Madi, Y., Minh, D. P., Sanz, F. J. E., Coquelet, C., Junqua, G., Heymes, F., Malhautier, L., Pré, P., Laforest, V., Lakhmi, R., Cornet, J.-F., Laboudigue, A., and Guisiano, J.-C., "Livre blanc `` Produire, Stocker et utiliser l'hydrogène ' '."

[2] Dematteis, E. M., Berti, N., Cuevas, F., Latroche, M., and Baricco, M., 2021, "Substitutional Effects in TiFe for Hydrogen Storage: A Comprehensive Review," Mater. Adv., **2**(8), pp. 2524–2560. https://doi.org/10.1039/D1MA00101A.

[3] Challet, S., Latroche, M., and Heurtaux, F., 2007, "Hydrogenation Properties and Crystal Structure of the Single BCC (Ti0.355V0.645)100−xMx Alloys with M = Mn, Fe, Co, Ni (x = 7, 14 and 21)," J. Alloys Compd., **439**(1), pp. 294–301. https://doi.org/10.1016/j.jallcom.2006.08.070.

[4] Matsushita, M., Monde, M., and Mitsutake, Y., 2013, "Experimental Formula for Estimating Porosity in a Metal Hydride Packed Bed," Int. J. Hydrog. Energy, **38**(17), pp. 7056–7064. https://doi.org/10.1016/j.ijhydene.2013.04.005.

[5] Okumura, M., Ikado, A., Saito, Y., Aoki, H., Miura, T., and Kawakami, Y., 2012, "Pulverization Mechanism of Hydrogen Storage Alloys on Microscale Packing Structure," Int. J. Hydrog. Energy, **37**(14), pp. 10715–10723. https://doi.org/10.1016/j.ijhydene.2012.04.061.

[6] Buschow, K. H., and Van Mal, H. H., 1972, "Phase Relations and Hydrogen Absorption in the Lanthanum-Nickel System," J. Common Met., **29**(2), pp. 203–210. https://doi.org/10.1016/0022-5088(72)90191-9.

[7] Sleiman, S., Shahgaldi, S., and Huot, J., 2024, "Investigation of the First Hydrogenation of LaNi5," Reactions, **5**(3), pp. 419–428. https://doi.org/10.3390/reactions5030021.

[8] Cao, X. X., Yang, F. S., Wu, Z., Wang, Y. Q., and Zhang, Z. X., 2013, "Experimental Study on the Hydrogen Storage Properties of $LaNi_5$ Alloy in Repeated Hydriding/Dehydriding Cycles," Adv. Mater. Res., **815**, pp. 25–30. https://doi.org/10.4028/www.scientific.net/AMR.815.25.

[9] Reilly, J. J., and Wiswall, R. H., 1974, "Formation and Properties of Iron Titanium Hydride," Inorg. Chem., **13**(1), pp. 218–222. https://doi.org/10.1021/ic50131a042.

[10] Dematteis, E. M., Dreistadt, D. M., Capurso, G., Jepsen, J., Cuevas, F., and Latroche, M., 2021, "Fundamental Hydrogen Storage Properties of TiFe-Alloy with Partial Substitution of Fe by Ti and Mn," J. Alloys Compd., **874**, p. 159925. https://doi.org/10.1016/j.jallcom.2021.159925.

[11] Benyelloul, K., Bouhadda, Y., Bououdina, M., Faraoun, H. I., Aourag, H., and Seddik, L., 2014, "The Effect of Hydrogen on the Mechanical Properties of FeTi for Hydrogen Storage Applications," Int. J. Hydrog. Energy, **39**(24), pp. 12667–12675. https://doi.org/10.1016/j.ijhydene.2014.05.190.

[12] Dematteis, E. M., Cuevas, F., and Latroche, M., 2021, "Hydrogen Storage Properties of Mn and Cu for Fe Substitution in TiFe0.9 Intermetallic Compound," J. Alloys Compd., **851**, p. 156075. https://doi.org/10.1016/j.jallcom.2020.156075.

[13] Johnson, J. R., and Reilly, J., 1977, "The Use of Manganese Substituted Ferrotitanium Alloys for Energy Storage," Proc. Int. Conf. Altern. Energy Sources Miami Beach Fla. 19771205 19771207. https://doi.org/10.2172/1004984.

[14] Modi, P., and Aguey-Zinsou, K.-F., 2019, "Titanium-Iron-Manganese (TiFe0.85Mn0.15) Alloy for Hydrogen Storage: Reactivation upon Oxidation," Int. J. Hydrog. Energy, **44**(31), pp. 16757–16764. https://doi.org/10.1016/j.ijhydene.2019.05.005.

[15] Zeng, L., He, J., Li, J., Luo, L., Xi, H., Yan, Y., Wu, C., Mu, S., Lan, Z., Wang, W., Zhu, D., and Chen, Y., 2024, "Enhancing the Hydrogen Storage Properties of Ti–Mn Alloys by Ti Occupying Mn Sites: An Experimental and Theoretical Study," ACS Sustain. Chem. Eng., **12**(15), pp. 5819–5830. https://doi.org/10.1021/acssuschemeng.3c07291.

[16] Li, C., Guo, H., Zheng, L., Yang, J., Ye, L., Liu, L., and Zhang, L., 2023, "Phase Equilibria of the Ti-Nb-Mn Ternary System at 1173K, 1273K and 1373K," Processes, **11**(2), p. 424. https://doi.org/10.3390/pr11020424.

[17] Liu, J., Sun, L., Yang, J., Guo, D., Chen, D., Yang, L., and Xiao, P., 2022, "Ti–Mn Hydrogen Storage Alloys: From Properties to Applications," RSC Adv., **12**(55), pp. 35744–35755. https://doi.org/10.1039/D2RA07301C.

[18] Gamo, T., Moriwaki, Y., Yanagihara, N., Yamashita, T., and Iwaki, T., 1985, "Formation and Properties of Titanium-Manganese Alloy Hydrides," Int. J. Hydrog. Energy, **10**(1), pp. 39–47. https://doi.org/10.1016/0360-3199(85)90134-X.

[19] Arnal, S., Maynadier, A., Laversenne, L., and Chapelle, D., 2025, "Underlying Causes of the Improved Storage Properties of $TiMn_{1,5}$ by Annealing Treatment," ACS Appl. Energy Mater., **8**(2), pp. 998–1005. https://doi.org/10.1021/acsaem.4c02527.

[20] Semboshi, S., Masahashi, N., and Hanada, S., 2001, "Degradation of Hydrogen Absorbing Capacity in Cyclically Hydrogenated TiMn2," Acta Mater., **49**(5), pp. 927–935. https://doi.org/10.1016/S1359-6454(00)00371-2.